Energy Deposition in Low-Power Coaxial Plasma Thrusters

R. M. Myers,* A. J. Kelly,† and R. G. Jahn‡
Princeton University, Princeton, New Jersey 08544

An experimental examination of energy deposition in self-field, coaxial plasma thrusters revealed that the thrust efficiency ranged from 2–9% and that the dominant losses resulted from electrode heating and propellant ionization. Sensible enthalpy and radiative losses were negligible. Thruster specific impulse increased with current, ranging from 550–1750 seconds. Spectroscopic studies of the plume plasma showed that the electron temperature ranged from 0.5–2.5 eV and that the dominant species were singly and doubly ionized argon. Attempts to raise thruster efficiency by increasing the chamber pressure resulted in reduced electrode losses and lowered I_{sp}, but the thrust efficiency decreased because of a current redistribution that lowered the thrust beyond expectations.

Nomenclature

A = surface area
A_{ik} = spontaneous emission coefficient from level i to k
ArI, ArII, ArIII = neutral, singly and doubly ionized argon
B = magnetic field strength
$E(p)$ = energy of pth level with respect to ground state
$E_i(p)$, $E_{ii}(p)$ = first and second ionization energies for pth level
e = electron charge
$g(i, p)$ = degeneracy of pth level for species i
h = Planck's constant
I_{sp} = specific impulse
I = intensity
J = total current
j_e, j = random thermal electron current and total current densities
$K(T_e)$ = equilibrium constant
k = Boltzmann constant, thermal conductivity [Eq. (14)]
M = atomic mass
$\dot{m}$ = mass flow rate
m_e = electron mass
$N_i(p)$ = number density of the pth level of species i
r_a, r_c = anode and cathode radii
T = thrust
T_e = electron temperature
u = velocity
V_{af} = anode fall voltage
α = ionization fraction [Eq. (9)], fraction thermionic current [Eq. (14)]
λ = wavelength
ν = frequency
ε = emissivity
ρ = mass density
σ = Stefan-Boltzmann constant [Eq. (14)], conductivity [Eq. (15)]
Φ_a, Φ_c = anode and cathode work functions

I. Introduction

An understanding of energy deposition processes in coaxial plasma thrusters is critical if they are ever to be used for spacecraft propulsion. Although many studies have shown the potential for high specific impulse,[1–3] all thrusters tested to date have suffered from low efficiency. This paper presents the results of a study directed at improving our understanding of the energy-loss mechanisms and their coupling to thruster geometry and operating conditions.

Coaxial plasma thrusters produce a high-velocity exhaust via electrothermal and/or electromagnetic processes. Loss mechanisms include resistive dissipation within the electrodes and plasma-electrode interactions; plasma losses due to unrecovered dissociation, ionization, internal modes (vibration, rotation), and random thermal energy; and divergence losses and radiation. Previous experimental studies have covered the gamut of power levels (up to 600 kW steady state,[4] up to 10 MW for 2 ms pulses[1]) but these are riddled with ambiguities introduced by unacceptably high tank pressures ($\geq 10^{-1}$ Pa), electrode and chamber surface temperature variations, or the presence of an applied magnetic field.[5,6] In addition, the lack of adequate diagnostics has precluded a comprehensive examination of energy deposition in these devices.

Following a description of the experimental facilities in Sec. II, results of performance measurements, plasma characterization, and electrode studies are presented in Secs. III, IV, and V, respectively. Throughout, an attempt is made to intrepret and correlate the measurements using currently accepted models. Finally, a summary of the major conclusions is given in Sec. VI. Details of the spectroscopic analysis are presented in the Appendix.

II. Experimental Facility and Thruster Design

The thrusters were mounted at the end of a 0.7-m copper pendulum in a 1.5-m-diam, 6-m-long, steel vacuum tank, the pressure of which was maintained below 0.07 Pa during testing. Current and propellant were passed to the pendulum through mercury pots and a flexible hose near the pendulum pivots. The thruster was powered by a customized 50-kW Miller welding supply (80 V open circuit) with a maximum current ripple of 0.5%. This supply permitted operation at currents up to 1250 A at 40 V. The arc was started by inserting a tungsten wire probe into the interelectrode region and discharging a 416 μF capacitor bank charged to approximately 3000 V between the probe and the anode.

Thruster performance measurements (thrust and efficiency) were obtained from the propellant mass flow rate, voltage, and thrust. Measurements of floating potential, cathode surface temperatures, and thruster body temperatures were used to estimate electrode losses. Plasma characteristics were ob-

---

Received Dec. 1, 1989; revision received Aug. 6, 1990; accepted for publication Sept. 12, 1990.

*Graduate Student; currently at Sverdrup Technology, NASA Lewis Research Center, Cleveland, OH. Member AIAA.

†Senior Research Engineer, Mechanical and Aerospace Engineering. Member AIAA.

‡Professor, Mechanical and Aerospace Engineering. Fellow AIAA.

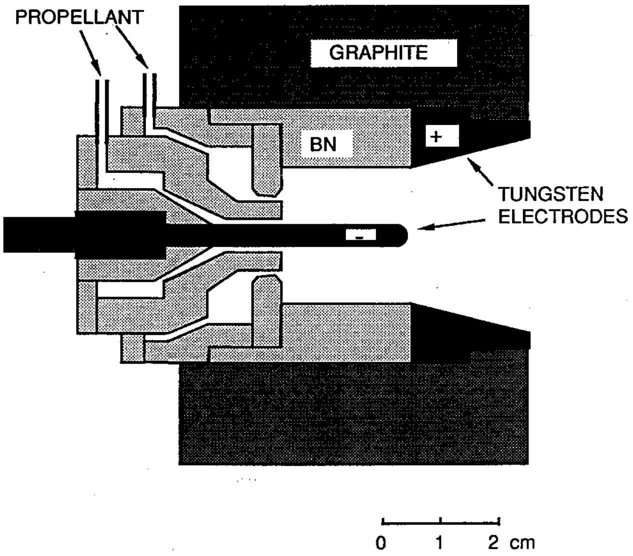

Fig. 1 Benchmark thruster configuration.

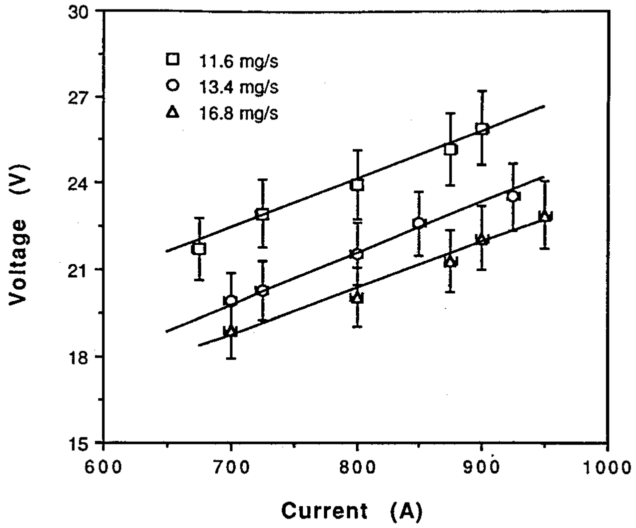

Fig. 2 Benchmark *V-J* characterisic for argon at three mass flow rates.

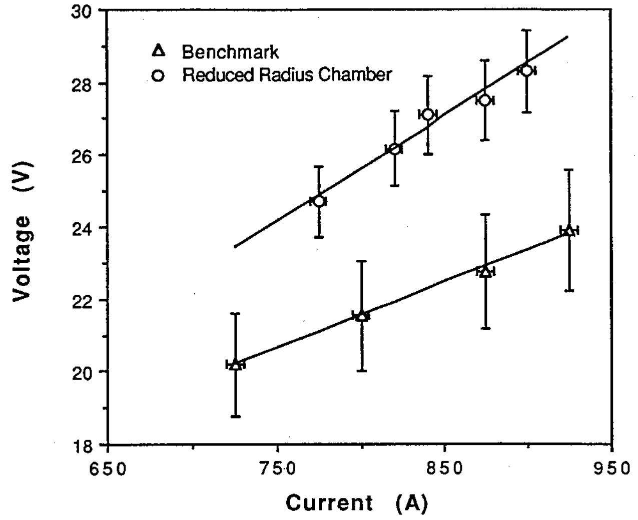

Fig. 3 *V-J* characteristic for two geometries at 13.4 mg/s argon.

tained from spectroscopic measurements at the exhaust plane and filter photography of the thruster chamber and plume.

The benchmark thruster, shown schematically in Fig. 1, consisted of a 0.48-cm-diam, 2.8-cm-long, 2% thoriated tungsten cathode extending from a boron nitride chamber and mass injection system. This was enclosed in a 10-cm-diam graphite cylinder that served as the main structural component, the anode conductor, and as a thermal radiator. Propellant was injected into the chamber from two independent plenna via annulli at the cathode base and at the midradius between the cathode and the chamber wall. Graphoil gaskets were used to prevent leakage between thruster components. The second geometry tested, the reduced chamber radius thruster, was identical in every respect to the benchmark geometry except for the chamber area, which was reduced by a factor of two by inserting a boron nitride cylinder into the bench mark chamber. This cylinder, which extended the length of the chamber, ended with 45-deg half-angle flare that merged with the upstream anode edge.

III. Performance Measurements

A. Voltage-Current Characteristics

Benchmark Geometry

Voltage and current were measured to ±0.25 V and ±5 A, respectively. Errors in these measurements result primarily from data scatter; experiments were performed several times to verify repeatability. It was shown previously[7] that the influence of propellant injection scheme on the voltage magnitudes was negligible. The voltage-current (*V-J*) characteristics and associated linear least-squares fits for argon at three mass flow rates with a 50:50 propellant split between the inner and midradius injection annuli are shown in Fig. 2. It is evident that decreasing the propellant flow rate increased the terminal voltage but did not change the slope of the *V-J* curve. For all conditions, the voltage increased approximately linearly with current level. Similar results were obtained for nitrogen propellant, although the voltage was slightly higher for nitrogen than for argon at the same mass flow rate.

Reduced Chamber Radius

Figure 3 shows that reducing the chamber radius (halving the chamber area) increased both the magnitude and the slope of the voltage for argon. The voltage increased by up to 5 V at high currents. The same effect, although less dramatic, was observed for nitrogen. Decreasing the chamber radius also appeared to influence the sensitivity to mass flow rate: reducing the flow rate from 13.4 mg/s to 11.5 mg/s in the reduced area thruster had a significantly more pronounced effect on the *V-J* characteristic than a similar change in the benchmark geometry.

B. Thrust, Specific Impulse, and Efficiency

Thrust was measured by monitoring the deflection of the pendulum arm. In-situ calibrations were obtained using a motor drive to suspend weights from a lever attached to the pendulum. Electromagnetic noise problems resulted in measurement errors of ≤5 mN for the benchmark geometry and ≤20 mN for the reduced chamber radius thruster.

Thrust measurements for the two thruster geometries are shown in Fig. 4. These data include two argon flow rates for both the benchmark and reduced chamber radius geometries. Thrust appeared to be independent of mass flow rate, ranging from 0.05–0.2 N for the benchmark geometry and from 0.05–0.12 N for the reduced chamber radius thruster. Superimposed on the thrust data are theoretical estimates of the self-field electromagnetic thrust, calculated from[2]

$$T = \frac{\mu_o J^2}{4\pi} \ln\left(\frac{r_a}{r_c}\right) = bJ^2 \tag{1}$$

where r_a was taken as either the average and maximum anode radii. Previous work[2,8] has indicated this relation is valid for

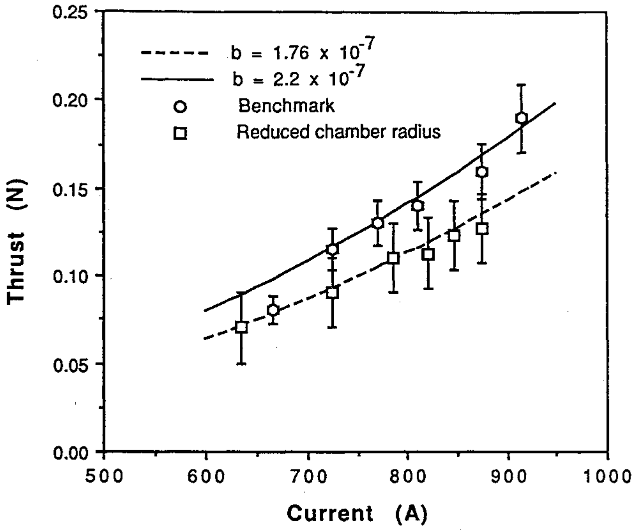

Fig. 4 Thrust-current characteristics for two geometries with argon propellant.

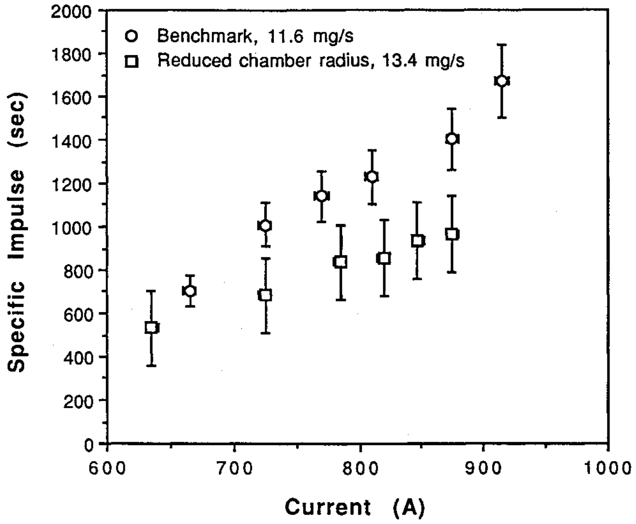

Fig. 5 Specific impulse vs current for two geometries with argon propellant.

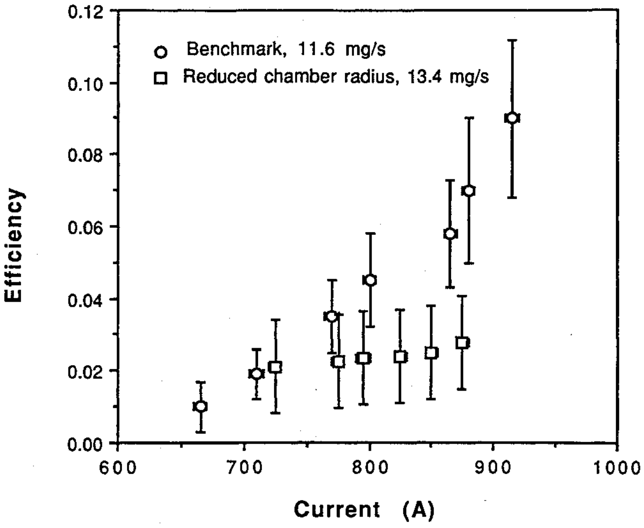

Fig. 6 Efficiency vs current for two geometries with argon propellant.

the operating conditions covered in this study. The magnitudes and trends for both geometries generally follow the theoretical curves, but the geometric constant *b* that best fits the data is lower for the reduced chamber radius thruster.

This observed decrease in thrust level for the reduced chamber radius thruster was most likely due to a redistribution of the current on the anode surface. Visual observation of the anode surface temperature distribution during testing indicated a current concentration at the anode lip with the benchmark geometry and at the anode base with the reduced chamber radius. These observations were substantiated by anode discoloration in these locations for the two geometries.

The highest resulting specific impulses for the two geometries are shown in Fig. 5. These correspond to mass flow rates of 11.6 and 13.4 mg/s for the benchmark and reduced radius thruster, respectively. The error bars include a 5% uncertainty in the mass flow rate; cathode erosion contributes less than 1% of the steady-state mass flow.[9] The highest I_{sp}, 1750 s, was obtained for the benchmark thruster at the lowest flow rate, 11.6 mg/s. Arc instabilities prevented operation of the reduced chamber radius thruster at flow rates lower than 13.4 mg/s or at currents above 850 A, so the maximum I_{sp} was correspondingly lower. It is important to note that, for argon propellant, the higher values of specific impulse cannot be explained by thermal acceleration, lending further support to the correlation with a self-field electromagnetic acceleration model. Estimates of the sensible enthalpy [Eq. (9)], which is the only thermal energy recovered at the low pressures in these devices, indicate that thermal acceleration can only play a significant role for specific impulses below ~500 s with argon.

The resulting thruster efficiencies, plotted as a function of current, are shown in Fig. 6. The efficiency increased sharply with current level for the benchmark thruster while remaining approximately constant for the reduced radius geometry. A peak efficiency of about 9% was reached with a mass flow of 11.6 mg/s. The peak efficiency with the reduced chamber radius thruster was about 2.5%. The primary effect of decreasing the chamber radius was to worsen thruster performance via an increased terminal voltage and a decreased thrust level.

IV. Plasma Characteristics

A. Plasma Species

Argon Propellant

A Spex 0.75-m spectrometer was used to photograph the plasma emission spectrum 3 mm in front of the anode exit plane. These photographs were centered at wavelengths of 340 nm, 430 nm, and 465 nm with a bandwidth of approximately 40 nm. Prominent lines between 328.5 nm and 366 nm were from singly and doubly ionized argon (ArII and ArIII), although a few faint neutral argon lines were identified. Doubly ionized argon was confined to the central regions of the discharge. Faint spectral lines from nitrogen and tungsten were identified, probably originating from the boron-nitride insulator and the cathode, respectively.

Nitrogen Propellant

The spectral ranges photographed were between wavelengths of 442.0 and 487.0 nm and 549.5 and 574.7 nm. Vibrational bands indicative of molecular nitrogen were predominant in the lower wavelength region for tests conducted at lower currents and higher mass flows (660 A and 13.6 mg/s, respectively). Singly ionized nitrogen lines were clearly visible, and no evidence of either doubly ionized nitrogen or molecular ions was found.

B. Electron Temperatures and Species Densities

Exhaust plane plasma characteristics were quantified using an Ikegami ITC-400 vidicon camera detector at the spectrometer photoplane. This system acquired 30 complete profiles

Table 1 Spectral lines and associated data for spectral measurements

λ, nm	$E(p)$, eV	$g(p)$	A_{ik}, s^{-1}
486.59	22.5	6	1.5×10^7
487.98	19.67	6	7.8×10^7
488.91	19.79	2	1.59×10^7
490.47	21.13	8	4.5×10^6
493.32	19.25	4	1.43×10^7
496.51	19.76	4	3.47×10^7
497.22	19.3	2	9.6×10^6

of all spectral lines used in the analysis every second. Spectra were monitored and stored continuously throughout the tests, including startup, steady-state, and shut-down phases of operation. Intensity calibrations were performed using a tungsten ribbon lamp precalibrated with a Leeds and Northrup optical pyrometer. Spectra were analyzed to obtain intensity profiles (using 80 radial points) using an AT&T Targa M8 frame grabber and Media Cybernetics Image-Pro software. Only results for argon are presented; the complexity of the nitrogen spectrum precluded detailed analysis of the line intensity measurements.

Seven singly ionized argon lines, listed along with the relevant atomic data[10] in Table 1, were used for these measurements. The intensity profiles were Abel-inverted using the algorithm proposed by Nestor and Olsen[11] to obtain the radial emission coefficient for each line. This technique was verified using various test functions, and yields reasonable values of the emission coefficient at intermediate radii; values at the plume axis and edge are suspect.

Electron Temperature

The electron temperature was calculated from a linear least-squares fit of a plot of

$$\ln\left(\frac{I_{ik} g_l \nu_{jl} A_{jl}}{I_{jl} g_i A_{ik} \nu_{ik}}\right) \quad \text{vs.} \quad \Delta E_{ij} \tag{2}$$

where T_e is the inverse of the line slope. Error estimates were obtained by combining the error in the measured intensities and the transition probabilities using a standard algorithm.[12]

Figure 7 shows the calculated radial variation of the electron temperature for the reduced chamber radius thruster with argon flow rates of 12 and 15 mg/s at a current level of 815 A. The effect of increasing the mass flow was similar to decreasing the current: at the higher flow rate (15 mg/s) the temperature profile had much stronger radial gradients and the magnitude was significantly lower (by ~1 eV at the higher radii) than for the lower mass flow. The temperature distribution was relatively flat for all conditions, and the influence of thruster geometry on the electron temperature was small.

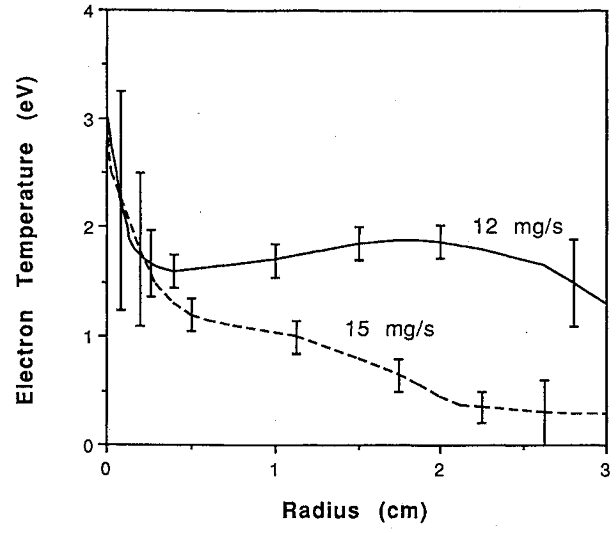

Fig. 7 Electron temperature vs radius for two argon flow rates.

Species Densities

A Saha-type ionization balance was used to estimate the electron density from the above data. The upper excited-state populations of singly ionized argon are related to the ground-state population of doubly ionized argon by[13]

$$\frac{N_{\text{ArIII}} N_e}{N_{\text{ArII}}(p)} = \frac{2g(\text{ArIII}, 1)}{g(\text{ArII}, p)} \left(\frac{2\pi m_e k T_e}{h^2}\right)^{1.5} \exp\left(\frac{-E_i(p)}{kT_e}\right) = K(T_e) \tag{3}$$

where $N_{\text{ArII}}(p)$ is the measured population of the pth level. The absence of data for neutral argon precluded the use of a similar Saha equation relating ArI to ArII, which restricted these calculations to regions where the dominant ionization balance is between ArII and ArIII. This point will be further discussed below.

To complete the formulation, we use charge conservation

$$N_e = N_{\text{ArII}} + 2N_{\text{ArIII}} \tag{4}$$

and relate the measured ArII excited-state density to the ground-state density of ArII by

$$\frac{N_{\text{ArII}}(p)}{N_{\text{ArII}}(1)} = f(T_e, N_e) \tag{5}$$

where $f(T_e, N_e)$ depends on the state of the plasma. This equation was used to calculate the total population of argon in Eq. (4), since for these plasma conditions the excited-state population is less than 5% of the total argon population. Thus, combining Eqs. (3–5), we obtain

$$\frac{1}{2}\left(N_e - \frac{N_{\text{ArII}}(p)}{f(T_e, N_e)}\right) N_e = N_{\text{ArII}}(p) K(T_e) \tag{6}$$

which is the equation to be satisfied for the measured $N_{\text{ArII}}(p)$ and T_e.

Two cases were considered: the first assumed that the excited-state populations were in thermal equilibrium (TE) and governed by the Boltzmann distribution:

$$f(T_e, N_e) = \frac{g(\text{ArII}, p)}{g(\text{ArII}, 1)} \exp\left(\frac{-E(p)}{kT_e}\right) \tag{7}$$

The second used a nonthermal equilibrium model (NTE), where $f(T_e, N_e)$ was evaluated using a 12-level ArII atomic model with approximate rate equations (see Appendix). The calculations were performed independently for each of the seven measured excited-state populations and the results averaged.

Typical results for both methods, along with the calculated N_e/N_{ArII}, are shown in Table 2 for the reduced chamber radius thruster. For all ionization levels up to 100% N_e/N_{ArII} should

Table 2 Calculated electron densities for benchmark thruster with 14.9 mg/s argon at 860 A (Densities in cm^{-3})

Radius, cm	T_e, eV	N_e (TE)	N_e (NTE)	N_e/N_{ArII} (NTE)	N_e/N_{ArII} (TE)
.2	1.3	4×10^{13}	3×10^{13}	1.7	2.5
.4	1.4	4×10^{13}	2.7×10^{13}	3	13
.6	1.35	3×10^{13}	2.5×10^{13}	1.5	8
.8	1.23	3×10^{13}	2×10^{13}	1.1	1.1
1.0	1.15	5×10^{13}	5×10^{13}	1.0	1.0

Table 3 Power lost to ionization and unrecovered sensible enthalpy

$\dot{m}$, mg/s	J, A	P_i, kW	P_i/P_t	P_{sh}, kW	$P_{\text{sh}}P_t$
10	700	0.38	0.03	0.12	0.008
	800	0.55	0.03	0.15	0.0083
	900	0.71	0.033	0.2	0.0095
15	700	0.35	0.024	0.18	0.012
	800	0.57	0.03	0.23	0.013
	900	0.7	0.03	0.30	0.013

equal one, if it is greater than one the plasma is partially doubly ionized. The electron densities predicted by the NTE and TE methods were very close, ranging from 2–4 × 10^{13} cm^{-3} (±1 × 10^{13} cm^{-3}) depending on the radius. The ratio of the electron density to the singly ionized argon density was considerably greater at low radii for the TE case due to the underprediction of the ground-state density when a Boltzmann distribution was assumed. Results for a test at a lower mass flow rate (12.3 mg/s) showed that while the electron density was insensitive to flow rate, the ratio N_e/N_{ArII} increased dramatically (by a factor of five). These results show that the plasma was partially double ionized in the central region of the plume, in agreement with the photographic spectral studies described earlier.

At radii larger than 1 cm, the calculated electron density began to increase. This was due to a combination of a sharp decrease in excited-state population and the forced balance (in the analysis) between singly and doubly ionized argon: for the given equations, the decreased density of singly ionized argon could only be accounted for via the formation of ArIII, with an associated increase in electron density. These results show that this balance was not the dominant cause of the observed ArII depletion at large radii; a more likely cause for the observed decrease in intensity is plume expansion. Recombination of ArII to ArI is not significant at the low plume densities.

The power associated with ionizing the argon propellant can be written

$$P_i = E_i\dot{m}_{\text{ArII}} + (E_i + E_{ii})\dot{m}_{\text{ArIII}} \tag{8}$$

where E_i and E_{ii} are 15.8 and 27.6 eV, respectively. The sensible enthalpy of the plasma is

$$h_s = \frac{5kT}{2M_i}(1 + \alpha) \tag{9}$$

where the electron and ion temperatures were assumed equal and the ionization fraction varies between 0 and 2 to account for the presence of ArIII. The order of this term was estimated using the maximum electron temperature measured for the given current. The power tied up in sensible enthalpy P_{sh} was obtained by multiplying h_s by the mass flow. Results of these power calculations for two mass flow rates and the associated fractions of the total thruster power are given in Table 3, which shows the combined ionization and sensible enthalpy powers are less than 4% of the input power. It is clear that the power required to create and maintain the fully ionized argon plasma at the flow rates considered was a small fraction of the total thruster power for these geometries and operating conditions.

V. Electrode Processes

A. Anode Processes

The net power lost to the anode can be written as

$$P_a = J_e\left(\Phi_a + V_{af} + \frac{5kT_e}{2e}\right) \tag{10}$$

where convection and internal ohmic heating were neglected.[14] The anode power P_a was evaluated using electron temperatures from the previous section, the work function of 2% thoriated tungsten (approximately 3.3 eV[15]), and measurements of the anode fall voltage. The latter were made using a floating probe, referenced to the anode, which was rapidly rotated to a position 3 mm above the anode surface. Probe rotation was accomplished using a Ledex rotary solenoid; the probe was removed undamaged after less than 0.1 s within the thruster. No significant differences were noted between measurement points along the anode, and testing showed that the anode temperature did not influence the fall voltage. The latter was shown using measurements taken immediately after startup (with a cold anode) and after the anode had reached ~2000 °C.

Measured floating potentials were converted to plasma potentials using[16]

$$\Delta V = \frac{kT_e}{2e}\ln\left(\frac{\pi m_e}{2M}\right) \tag{11}$$

which, while relatively crude given the flow complexity, was adequate for the purposes of this study. The electron temperature was ~0.8 eV near the anode surface (Sec. IV), yielding a correction of 4.3 V for argon. This correction was used for all measurements, although no T_e measurements were available for nitrogen.

Typical results for argon and nitrogen propellants at the same flow rate (13.4 mg/s) are compared in Fig. 8. For all tests, the fall voltage increased with current level and decreased slightly with increasing mass flow rate. The anode fall was significantly smaller with nitrogen at the lower currents (as low as 9 V), but the difference decreased above 750 A. Reducing the thruster chamber radius decreased the fall voltage by approximately 3 V. This geometric effect is most pronounced when comparing the ratios of the fall-to-total thruster voltages as is done in Fig. 9. The voltage fraction associated with the anode fall was about 20% higher with the benchmark thruster. These results indicate that the dominant source of the terminal voltage rise observed when the current is increased (Figs. 2 and 3) is the anode fall, not the plasma drop.

These measurements show that for all operating conditions the anode was by far the largest energy sink in these thrusters. The power fraction invested in the anode is plotted vs thruster power in Fig. 10, where the electron current was assumed equal to the thruster current. Between 80 and 90% of the total power was deposited into the anode with the benchmark geometry, and between 65 and 80% with the reduced chamber radius thruster. Independent confirmation of this conclusion was provided by temperature measurements of the graphite

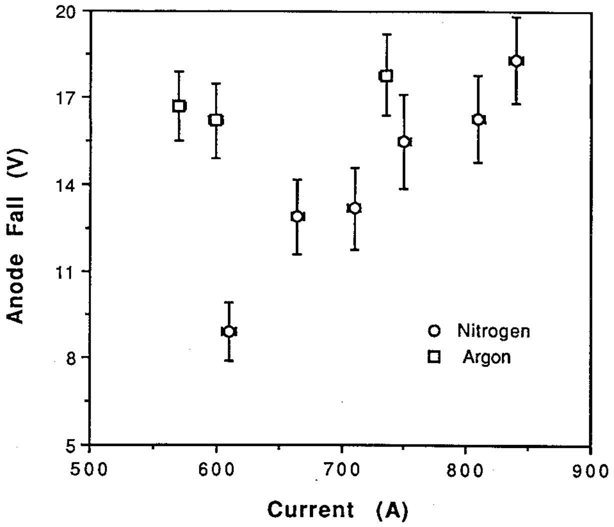

Fig. 8 Anode fall voltage vs current for benchmark thruster with argon and nitrogen propellants at 13.4 mg/s.

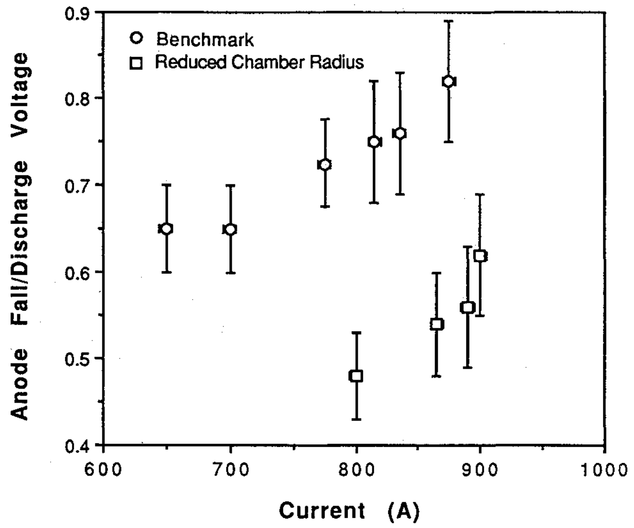

Fig. 9 Anode fall fraction vs current for two geometries with 15 mg/s argon.

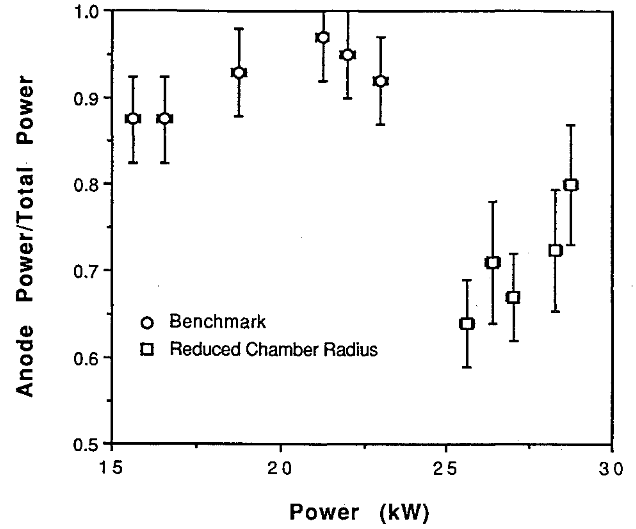

Fig. 10 Anode power fraction vs total thruster power for two geometries with 15 mg/s argon.

block surrounding the anode. Results of a thermal analysis[17] showed that the measured temperatures can only be explained if over 80% of the thruster power is deposited into the anode.

The fall-voltage measurements represent the integral of the potential distribution between the anode surface and the probe. This distribution includes the sheath region (on the order of a few Debye lengths thick) and any other near-wall processes that influence the potential. The latter include conductivity gradients due to temperature and density gradients resulting from wall cooling and recombination. The sheath contribution can be estimated from

$$-V_a = \frac{kT_e}{e} \ln\left(\frac{j_e}{j}\right) \tag{12}$$

This relation has been used by Hugel[18] to explain anode power deposition in MPD thrusters. The thermal electron current is given by the product of the thermal electron flux and the electron charge

$$j_e = \frac{eN_e}{4}\sqrt{\frac{8kT_e}{\pi m_e}} \tag{13}$$

Using electron densities and temperatures from Sec. IV, the thermal electron current density at the anode is estimated to be 70 A/cm^2. Assuming a uniform current distribution over the anode, the total current density ranges from 10–38 A/cm^2 over the stable current range (500–1000 A). Under these conditions the sheath voltage is negative, ranging from −1 V at 500 A to −0.5 V at 1000 A. However, as discussed in Sec. III, there was evidence of nonuniform anode current attachment with both geometries studied. In addition, the radial pumping force caused by axial current conduction may have reduced the electron density in the anode region. It thus seems possible that the sheath voltage was actually positive, since only a factor of two difference in the current density ratios was required to cause this change. At this point, however, there is insufficient data to establish the dominant source of the 10–20 V anode fall voltages measured in the experiments.

B. Cathode Processes

The net power lost to a cathode with a steady temperature distribution can be estimated from the net outflow of energy from the cathode[9]

$$P_c = \int_A (j_e \Phi_c \alpha_e + \varepsilon \sigma T_c^4 - k \nabla T_c)\, \mathrm{d}A \tag{14}$$

where convection and evaporation were neglected. The latter was justified on the basis of erosion measurements for these thrusters.[9] The surface temperature distribution was measured using filtered video photography calibrated using a tungsten ribbon lamp to ±50 °C. Details of the measurement techniques and results have been presented elsewhere.[9]

Typical results for the temperature measurements are shown in Fig. 11. A comparison of the thermionic current, calculated from Richardson's equation, and the measured current levels, showed that thermionic emission adequately explained the cathode current conduction for a cathode work function of 4.5 eV (pure tungsten). This is not surprising since at the measured temperatures thorium will be rapidly depleted from

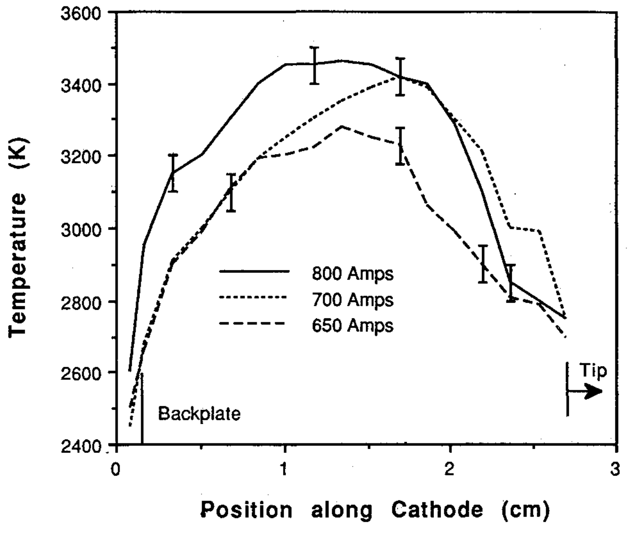

Fig. 11 Cathode temperature distribution for three current levels and 12 mg/s nitrogen flow rate.

Table 4 Cathode power loss calculated from temperature measurements and calculated thermionic currents (Φ_c = 4.5 eV); 11.5 mg/s argon

J, A	Electron Cooling, kW	Radiation, kW	Conduction, kW	P_c/P_t
800	2.1	1.03	0.12	0.15
700	1.3	0.88	0.15	0.09
650	0.66	0.78	0.16	0.11

Table 5 Magnetic Reynolds number R_{ml} and magnetic force number S for kilowatt- and megawatt-power level thrusters

Power level	$J^2/\dot{m}$, kA^2-s/g	R_{ml}	S
20 kW	10–90	0.05–1	0.004–0.1
1 MW	10–90	0.05–0.7	0.06–0.1

the surface. Equation (14) was evaluated by assuming the current to be fully thermionic, and calculating heat-conduction and radiation terms (the emissivity was measured to be 0.4[9]) using the temperature data. As shown in Table 4, the cathode power loss is between 10 and 15% of the total thruster power.

VI. Summary and Implications

Experimental measurements of performance, plasma characteristics, floating potentials, and thruster surface and body temperatures in two low-pressure geometries confirmed that the plasma energy balance was dominated by kinetic energy, ionization, and sensible enthalpy, but clearly showed that the anode was the largest thruster energy sink. Thrust increased with current level, and the specific impulse ranged from 550–1750 s. The magnitude and behavior of thruster-performance parameters indicate that the dominant plasma acceleration mechanism was electromagnetic. Floating potential and thruster temperature measurements showed that between 65 and 80% of the thruster power was deposited into the anode. In decreasing order, the remaining sinks were the cathode (10–15%), thrust (2–10%), ionization (2–3%), and sensible enthalpy (~1%). Although the plasma was optically thin, radiation losses did not contribute significantly due to the low plasma density and temperature. Decreasing the chamber radius did result in reduced electrode losses, but the total efficiency decreased due to a redistribution in thruster current.

These results also bear on the scaling characteristics of coaxial plasma thrusters. Comparing these data with those obtained for thrusters of similar geometry operated at megawatt-power levels[1,2,14] over the same range of the ratio $J^2/\dot{m}$ (which is proportional to specific impulse), we find that for both cases plasma acceleration is electromagnetic, the gas is highly ionized, the electron temperature is between 0.5 and 2.5 eV, and the electron densities are between 10^{13} and 10^{14} cm^{-3}. In addition, the anode fall voltages are similar (10–30 V). These data show that certain aspects of thruster behavior can be scaled to radically different power levels, a conclusion with important implications for the development of high-power, steady-state plasma thrusters because of the high cost of developing test facilities for these devices. Specifically, estimates of the magnetic Reynolds number R_{ml} and the magnetic force number S, defined by[19]

$$R_{\mathrm{ml}} = \mu \sigma u l, \qquad S = \frac{B^2}{\mu \rho u^2} \tag{15}$$

and shown in Table 5, indicate that the dynamics of plasma acceleration may be similar in the quasisteady megawatt-class thrusters and the kilowatt-class devices studied here. In addition, the magnitudes of the anode fall voltages are comparable in both low- and high-power devices. However, anode losses do not play a dominant role in megawatt-class thrusters due to the very large voltage drops across the plasma, which shows that the thrust efficiencies are quite different for the two power ranges.

Appendix

A. Simplification of the Rate Equation

The steady-state equations for the bound electronic states were simplified using the method proposed by Suckewer.[20,21] The time scales for ionization and recombination are long compared to bound-state interactions so they need not be included. Neglecting heavy-particle inelastic collisions and stimulated emission (both good assumptions for these plasmas) and solving for the density of level i, we obtain[22]

$$N = \frac{\Sigma_{k<i} N_e N_k S^{I}_{ik}}{\Sigma_{k<i} A_{ik} + N_e S^{II}_{ik}} + \frac{N_e \Sigma_{k>i}(N_k S^{II}_{ki} - N_i S^{I}_{ik}) + \Sigma_{k>i} N_k A_{ki}}{\Sigma_{k<i} A_{ik} + N_e S^{II}_{ik}} \tag{16}$$

where S^{I}_{ik} and S^{II}_{ik} are the electronic collision excitation and deexcitation rates, respectively. The first term in this equation includes transitions to and from levels below i, and the second involves interactions with levels above level i. For most cases of interest, the first of these terms is much larger than the second and can be neglected. This condition was checked a posteriori. Introducing

$$\eta_{ik} = \frac{N_e S^{II}_{ik}}{\Sigma_{k<i} A_{ik}} \tag{17}$$

the Holstein radiative escape factor[13] level i, τ_i, and using the Klein-Rosseland relation[23] to relate the collisional reaction rates, the equations reduce to

$$N_i = \frac{\Sigma_{k<i} N_k \eta_{ik} \dfrac{g_i}{g_k} \exp\left(\dfrac{-\Delta E_{ik}}{kT_e}\right)}{\tau_i + \Sigma_{k<i} \eta_{ik}} \tag{18}$$

The equations are solved sequentially, starting from the ground level, with $N_1 = 1$. The radiative escape factor was iteratively calculated for resonance radiation and set to unity for all other transitions. The influence of convective effects was checked at the same time as the second term in Eq. (16) and they were found to be negligible.[24]

B. Atomic Model and Collision Cross Sections

The ionized argon atom was approximated by a 12-level model. The properties of each level were calculated using

$$\bar{g}_j = \Sigma_i g_i, \qquad \bar{E}_i = \frac{\Sigma_k E_k g_k}{\Sigma_k g_k}, \qquad \bar{A}_{ik} = \frac{\Sigma_{jl} A_{jl} g_j}{\Sigma_j g_j} \tag{19}$$

with data from Wiese et al.[10] Collision cross sections for excitation were taken from Drawin.[25] Comparisons of the calculated cross sections with available data showed good agreement,[24] and a sensitivity analysis showed the influence of forbidden transitions to be negligible. The rate coefficients are calculated by numerically integrating over a Maxwellian distribution function at the measured electron temperatures and used to evaluate Eq. (17) for all transitions. An iterative procedure was used to determine the electron density from Eqs. (18) and (8) in the text.

Acknowledgments

This research was supported, in part, by the National Aeronautics and Space Administration under Contract 954997 and grants from Rocket Research, Inc., Hercules Aerospace Company, and the U.S. Department of Energy Plasma Physics Laboratory, Princeton, New Jersey.

References

[1] Merfeld, D. J., Kelly, A. J., and Jahn, R., "MPD Thruster Performance: Propellant Distribution and Species Effects," *Journal of Propulsion and Power*, Vol. 2, No. 4, July–Aug. 1986, pp. 317–322.

[2] Gilland, J., "The Effect of Scale upon MPD Thruster Performance," M.S. Thesis, Princeton, Univ., NJ, March 1988.

[3] Toki, K., Shimizu, Y., and Kuriki, K., "Application of MPD Thruster Systems to Interplanetary Missions," *Journal of Propulsion*

and Power, Vol. 2, No. 6, Nov.-Dec. 1986, pp. 508–512.

[4]Merke, W. D., et al., "Nozzle-Type MPD Thruster Experimental Investigations," *Proceedings of the 20th International Electric Propulsion Conference*, IEPC-88-028, October 1988, pp. 169–179.

[5]Connolly, D., et al., "Tests of Permanent Magnet and Superconducting MPD Thrusters," AIAA Paper 71-696, July 1971.

[6]Arakawa, Y., and Saso, A., "Steady-State Permanent Magnet MPD Thruster," AIAA Paper 87-1021, May 1987.

[7]Myers, R., Kelly, A. J., and Jahn, R. G., "Electrothermal-Electromagnetic Hybrid Thruster Research," AIAA Paper 87-1018, May 1987.

[8]Hugel, H., Kruelle, G., and Peters, T., "Investigations on Plasma Thrusters with Thermal and Self-Magnetic Acceleration," *AIAA Journal*, Vol. 5, No. 3, March 1967, pp. 551–561.

[9]Myers, R., Suzuki, N., Kelly, A. J., and Jahn, R. G., "Cathode Phenomena in a Low-Power, Self-Field MPD Thruster," AIAA Paper 88-3206, July 1988; also "Cathode Phenomena in a Low-Power Magnetoplasmadynamic Thruster," *Journal of Propulsion and Power*, Vol. 7, No. 5, Sept.-Oct. 1991, pp. 760–766.

[10]Wiese, W., et al., *Atomic Transition Probabilities*, NBS Vol. 22, No. 2, U.S. Government Printing Office, Washington, D.C., 1969.

[11]Nestor, O., and Olsen, H., "Numerical Methods for Reducing Line and Surface Probe Data," *SIAM Review*, Vol. 2, No. 3, July 1960, pp. 200–207.

[12]Bevington, P., *Data Reduction and Error Analysis for the Physical Sciences*, McGraw-Hill, New York, 1969, Chap. 4.

[13]McWhirter, R., "Spectral Intensities," *Plasma Diagnostic Techniques*, edited by R. Huddlestone and S. Leonard, Academic Press, New York, 1965, pp. 201–264.

[14]Oberth, R., "Anode Phenomena in High Current Discharges," Ph.D. Thesis, Princeton Univ., NJ, 1970.

[15]Rieck, G., *Tungsten and Its Compounds*, Pergamon Press, New York, 1967, Chap. 2.

[16]Chen, F., "Electric Probes," *Plasma Diagnostic Techniques*, edited by R. Huddlestone and S. Leonard, Academic Press, New York, 1965, pp. 113–199.

[17]Smith, W. W., private communication, Rocket Research Co., Redmond, WA, Oct. 1986.

[18]Hugel, H., "Effect of Self-Magnetic Forces on the Anode Mechanism of a High Current Discharge," *IEEE Transactions on Plasma Science*, Vol. PS-8, No. 4, Dec. 1980, pp. 437–442.

[19]Sutton, G., and Sherman, A., *Engineering Magnetohydrodynamics*, McGraw-Hill Co., New York, 1965, Chap. 8.

[20]Suckewer, S., "Excitation and Ionization of Atoms and Ions in a Nonthermal Plasma," *Journal of Physics*, Vol. B3, Jan. 1970, p. 380.

[21]Suckewer, S., "Population of Excited Levels of Atoms and Ions: Electron Temperature and Density from Relative Line Intensities of the Ions CIV, NV, and OVI," *Physics Review*, Vol. 170, No. 1, 5 June 1968, pp. 239–244.

[22]Myers, R., "Energy Deposition in Low Power Coaxial Plasma Thrusters," Ph.D. Thesis, Princeton Univ., NJ, June 1989.

[23]Oxenius, J., *Kinetic Theory of Particles and Photons*, Springer-Verlag, New York, 1986, Chap. 2.

[24]Myers, R., "Electric Propulsion Lab. Progress Rept.," Princeton Univ., NJ, MAE 1776.08, Aug., 1987.

[25]Drawin, H., "Collision and Transport Cross Sections," EUR-CEA-FC-383; March 1966.